Article

Pore Variation Characteristics of Altered Wall Rocks in the Huize Lead–Zinc Deposit, Yunnan, China and Their Geological Significance

Yanglin Li [1], **Zhigang Kong** [1,*], **Changqing Zhang** [2], **Yue Wu** [3], **Xue Yang** [4], **Yu Wang** [1] **and Gang Chen** [2]

[1]   Faculty of Land Resource Engineering, Kunming University of Science and Technology, Kunming 650093, China
[2]   MNR Key Laboratory of Metallogeny and Mineral Assessment, Institute of Mineral Resources, Chinese Academy of Geological Sciences, Beijing 100037, China
[3]   College of Resources and Environment, Yangtze University, Wuhan 430100, China
[4]   Sichuan Huili Lead & Zinc Co., Ltd., Huili 615100, China
*   Correspondence: zhigangkong@kust.edu.cn; Tel.: +86-159-2512-4696

Abstract: The porosity and permeability of the rock surrounding lead–zinc deposits are key factors for controlling the migration and precipitation of ore-forming hydrothermal fluid. In this paper, the Huize super-large lead–zinc deposit was taken as the case study, and variations in the porosity and permeability of the wall rocks and their relationship with the orebody were analyzed by using CT scanning technology. The experimental results showed that the average pore radius of dolomite with a decreasing distance to the orebody ranged from 1.60 to 1.65 μm, increasing to 1.77~2.05 μm. The CT porosity increased from 2.76%–2.81% to 3.35%–3.99%. The average pore throat length decreased from 29.57–39.95 μm to 13.57–16.83 μm. In the research, it was found that the hydrothermal fluids rich in chemical elements changed the properties of the surrounding rocks. Temperature rise will lead to dolomitization of limestone and recrystallization of dolomite. This process led to an increase in the porosity of the wall rocks. During the formation of the orebody, the metal minerals in the hydrothermal fluid entered the pores of the rock. As a result, the pore radius and pore volume of the wall rocks were reduced, along with the pore throat radius and pore throat length. Therefore, the wall rock pores near the orebody were isolated from each other, and the permeability of the surrounding rock decreased. The variation characteristics for the porosity and permeability of the dolomite at various distances from the mine can be used to discover orebodies.

Keywords: porosity; permeability; lead–zinc ore; Huize; altered wall rocks

1. Introduction

The border area of Sichuan, Yunnan and Guizhou on the southwest edge of the Yangzi Platform in China is an area with abundant MVT Pb–Zn ore [1]. The lead and zinc ores in this area are mostly comprised of thick carbonate formations. The deposition ages of the ore-bearing strata range from the Sinian to the Permian. Among them, the Dengying Formation of the Upper Sinian and the Baizuo Formation of the Lower Carboniferous are the most important ore-bearing strata [2,3]. Scholars have found that MVT deposits are always formed in the dolomite. For example, Davis [4] suggested that the mineralization in the Viburnum Trend lead belt in southeastern Missouri, USA occurred mainly at the dolomitic boundary of the Cambrian Bonneterre Fm. Davies and Smith [5] and Machel and Lonnee [6] suggested that hydrothermally altered dolomite formed at higher temperatures than limestone. The wall rocks were heated during the migration of the mineralized hydrothermal fluid. This process promoted the dolomitization of the limestone. Some Chinese scholars have carried out research on the spatial relationship between the MVT-type Pb–Zn ore and dolomitization. Zhang et al. noted that the dolomite has a high porosity

and permeability, which may be a primary reason why lead–zinc ore deposits preferentially occur in dolomite rock [1]. The porosity and permeability of deeply buried dolomite are usually better compared to limestone at the same depth [7]. Although some scholars realize that the porosity and permeability may be an important factor affecting mineralization, they have not studied this problem quantitatively.

Significant research has been carried out on the various deposits in the Sichuan, Yunnan and Guizhou areas [8–12]. The research has focused on the age of the mineralization, the geochemical characteristics of the ore and wall rocks, the source of the mineralized material, the regional tectonic evolution and the tectonic environment of the mineralization [11,13–17]. Han et al. [18] concluded that the Huize Pb–Zn ore is obviously controlled by tectonics and lithology through tectonic geology, mineral deposit geology and geochemistry, and they proposed the tectonic–fluid penetration mineralization model [9]. Li et al. [19] concluded from an isotopic geochemical study that the ore-forming metals in the Huize Pb–Zn field were from multiple sources, mainly derived from the enclosing carbonate strata, and the reduced sulfur was mainly derived from the reduction in the marine sulfate in the formation. Zhang [20], on the other hand, concluded that the mineralized metals were derived from basement rocks and Emeishan basalts, in addition to the enclosing carbonate strata, and were characterized by different sources of metallogenic elements. Han et al. [21] concluded that the mineral control structure of the Huize Pb–Zn deposit was "stepped". Minimal work has been carried out to correlate the physical properties, such as the porosity and permeability of the wall rocks and ore bodies. The rock pore volume determines the porosity while the pore throat characteristics determine the permeability. Together, the porosity and permeability determine the ability for porous media to move through the rocks [22].

To date, only Wang [23] has carried out tensile resistance and compression resistance tests of the dolomite and limestone in the Huize lead–zinc mine. In order to verify whether the porosity is indeed effective for ore control, this paper, based on a field survey and sampling, combines the previous research and applies rock CT scanning technology. Based on the scanning results of the rock slices, the porosity, permeability and other physical parameters of the dolomite in different alteration zonings of the Huize lead–zinc deposit were studied, and the indicative effects of these physical parameters on the mineralization center were analyzed.

2. Regional Geological Background

The Sichuan–Yunnan–Guizhou Pb–Zn ore field is located at the southwest region of the Yangzi Massif [10,24,25], the transitional zone between the Gondwana and the Laurasia. This area developed intensive structures that provide suitable conditions for mineralization [14,26]. The distribution of the lead–zinc deposits in this area is closely related to the faults. The major fault zones in the region are the Anninghe, Mile–Shizong, Xiaojiang and Weining–Shuicheng faults (Figure 1B). The Anninghe fault is more than 500 km long and nearly NS-trending. It is the boundary fault between the Kangding–Yunnan uplift zone and the Huili–Kunming subsidence zone. It is a trans-crustal fault with an early formation. It cuts through the sedimentary and basement strata and has an obvious control effect on the magmatic activity. The Mile–Shizong fault, which strikes NE, is a compression-twisted fault with a length of more than 250 km. This fault controls the intrusion and eruption of basic rocks in the Emeishan volcanic province. It was active during the Mesozoic Era. The Xiaojiang fault zone is NS-trending with a length of more than 400 km. It is still an active fault and has formed multiple secondary faults. The Weining–Shuicheng fault is a concealed fracture, which is not obvious on the surface, and strikes roughly NW. This fault was activated during the later Caledonian Era. These major faults and their secondary faults together constitute the tectonic framework of the region. Many lead–zinc deposits were formed and distributed near them [15].
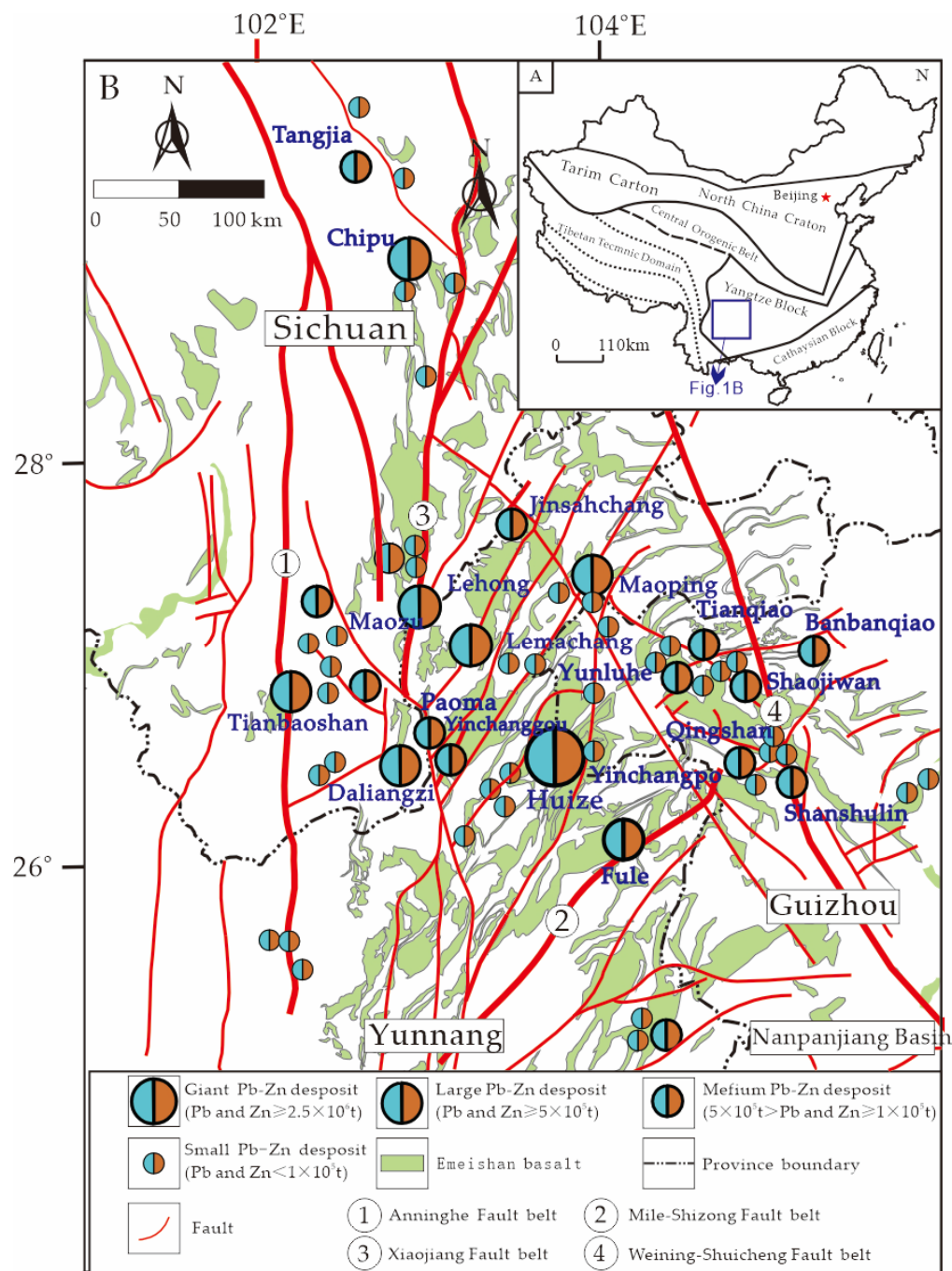
Figure 1. (**A**) Simplified tectonic map of South China (modified from [27]); (**B**) regional geological map of the Sichuan–Yunnan–Guizhou Pb–Zn triangle area (modified from [26]).

The lead–zinc deposits in this area are characterized by strata of multiple ages, but the location distribution is relatively concentrated, primarily in the northwest Guizhou, northeast Yunnan and southeast Sichuan regions [28]. The Pb–Zn deposits developed in the Sinian to Triassic strata (Table 1) and are concentrated in the carbonate strata. The ore-bearing stratigraphic lithology is mainly dolomite [2] and partly dolomitic limestone, in which large and medium-sized Pb–Zn deposits are located (Table 1). The controlling effect of lithology on the mineralization is obvious.

Table 1. Statistical table of the main host strata of the Pb–Zn deposits in the Sichuan–Yunnan–Guizhou area (modified from [29]).

Ore-Bearing Stratigraphy and Lithology of Different Ages	Large Scale	Medium Type	Smaller	Mining Sites	Mineralization Point	Representative Deposits
Triassic marlstone and limestone					3	Mine site only
Permian dolomitic limestone	1		3	9	8	Fule
Carboniferous medium-coarse crystal dolomite	2	3	13	39	12	Huize, Maoping
Upper Devonian medium-coarse crystalline dolomite	1	1	7	20	30	Zhaotong
Silurian limestone with sandy mudstone		1	5	3	5	Zhaziping
Ordovician dolomite		2	2	9	26	Butao
Upper Sinian–Lower Cambrian dolomites	3	8	18	54	96	Daliangzi, Jinsha, Maozu, Tianbaoshan

Although the Pb–Zn deposits in the area were formed during the Sinian to the Neopaleozoic and even in the Mesozoic periods, only a few are primary ore-bearing strata, such as the Upper Sinian Dengying Formation dolomite, Lower Cambrian Yuhucun Formation dolomite and Carboniferous Baizuo Formation dolomite (Figure 2). These three sets of strata host approximately 62% of the Pb–Zn deposits and 70% of the Pb–Zn resource reserves in the region (Figure 2). According to the lithology of the ore-bearing strata, the lead–zinc deposits in Sichuan, Yunnan and Guizhou can be divided into three types. The first type developed in the Upper Sinian Dengying Formation siliceous dolomite, the second type in the Lower Cambrian Yuhucun Formation phosphorus rock and phosphorus-bearing siliceous rock and the third type in the dolomite and dolomitic limestone of the Late Paleozoic Era (below the Emei Mountain basalt formation, including the Lower Carboniferous Baizuo Formation and the Lower Permian Maokou Formation) [10,24]. The Huize lead–zinc deposit belongs to the third type. The age of the ore-bearing strata in this region gradually becomes younger from west to east, and the ore-bearing rocks transition from siliceous rocks to carbonate rocks. Regionally, the carbonate rocks in the ore-bearing formation were formed in a variety of lithofacies environments, including tidal flats, closed platforms, semi-closed platforms, open platforms and lagoon facies, which do not have the uniqueness of lithofacies selection [30].
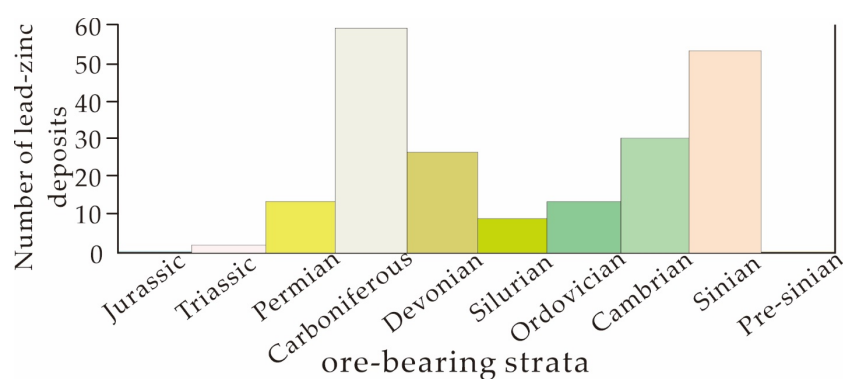
Figure 2. Statistics of the wall rocks strata of the MVT lead–zinc deposit in Sichuan, Yunnan and Guizhou (modified from [31]).

3. Geology of the Huize Lead–Zinc Deposit

3.1. Strata

The Huize Zn–Pb deposit is located in the southwest region of the Yangtze block in the eastern Kangdian oldland. The Zhaotong–Qujing fault is to the east of the Huize lead–zinc deposit and the Xiaojiang deep-seated fault zone is to the west [21]. The sedimentary strata in the mining area are dominated by carbonates and clastic rocks deposited from

late Neoproterozoic Era (late Sinian) to early Permian period. In addition, the late Permian Emeishan basalts developed in the northwestern part of the mining area (Figure 1).

The ore-bearing strata of the Huize Pb–Zn deposit are mainly in the Lower Carboniferous Baizuo Formation [32]. The upper part is comprised of light gray–white crystalline dolomite. The lower part is comprised of light gray dolomite limestone [33]. The Weining Formation of the Middle Carboniferous is another ore-bearing stratum of the Huize Pb–Zn deposit. The lithology is comprised of dolomite limestone and bioclastic limestone. The dolomite in the ore-bearing part is silicified, and the wall rocks near the orebody developed large geodes due to recrystallization. Due to this phenomenon, the crystal holes become smaller the farther they are from the orebody, and there was only a weak alteration in the wall rocks located far from the orebody.

3.2. Geological Features of the Ore Bodies

There are two main ore blocks in the Huize lead–zinc mine, which are distributed in the NE direction along the Qilinchang and Kuangshanchang faults (Figure 3) [29,34]. The shape of ore body is small vein, flat columnar, cystic, tubular, network-veined and stratiform-like. The stratiform-like orebody is controlled by the NE-trending interlayer fracture zone [21]. The orebody occurs in an interbedded fracture zone, and the extension length along the dip is longer than that along the strike. The ore bodies in some areas have the characteristics of a multi-layer output [34].
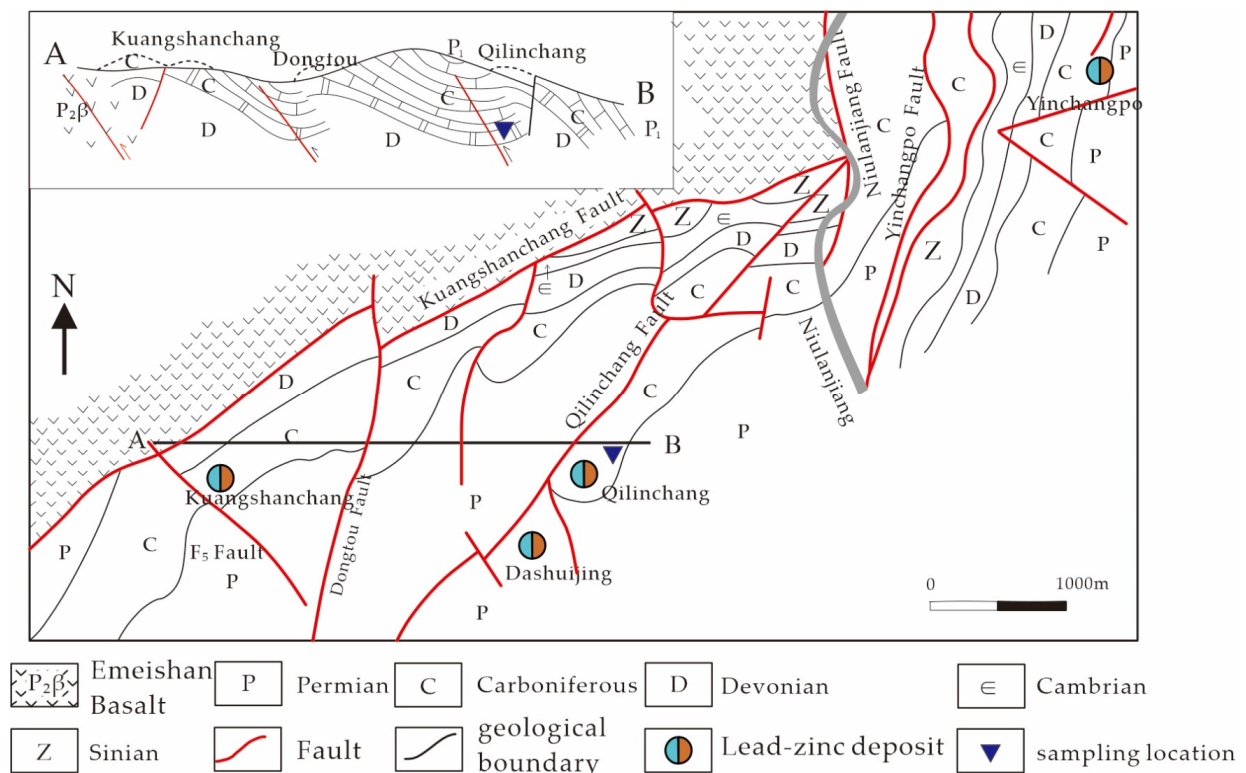

Figure 3. Geological map of the Huize lead–zinc deposit (modified from [29]). A, B: a geological section, including the mining area location, geological information and sampling location.

3.3. Mineral Assemblage

The metallic minerals in the mining area are mainly galena, sphalerite and pyrite. These metal minerals exist in the lead–zinc ore bodies, which have two forms Figure 4a shows the first form of the orebody. The contact line between the orebody and the dolomite was sharp and was formed by filling the ore-forming hydrothermal solution into the dolomite. The mineralization of another type of orebody occurred in the dolomite fracture zone, and there were fragments of dolomite in the orebody, as shown in Figure 4b. There

were differences in the morphology of the two types of ore bodies, but the morphological characteristics of the two types of ore bodies combined with the characteristics under the mineral microscope indicated that the mineralization occurred after the dolomitization. As for the period of the mineral formation, the pyrite was the earliest, sphalerite was the second and galena was the third. The crystal morphology of the pyrite was mainly non-euhedral. Figure 4c–f shows that part of the pyrite was replaced by the sphalerite and galena. In Figure 4c, it can be observed that the galena replaced the sphalerite and pyrite, and black triangular pores in the galena can also be seen. It can be observed in Figure 4d that the sphalerite replaced the pyrite and that the sphalerite contained some fragments of pyrite. It can be observed in Figure 4e that the sphalerite was wrapped in pyrite, and finally that the galena replaced part of the sphalerite. Figure 4f shows that the galena filled the interior of the pyrite.
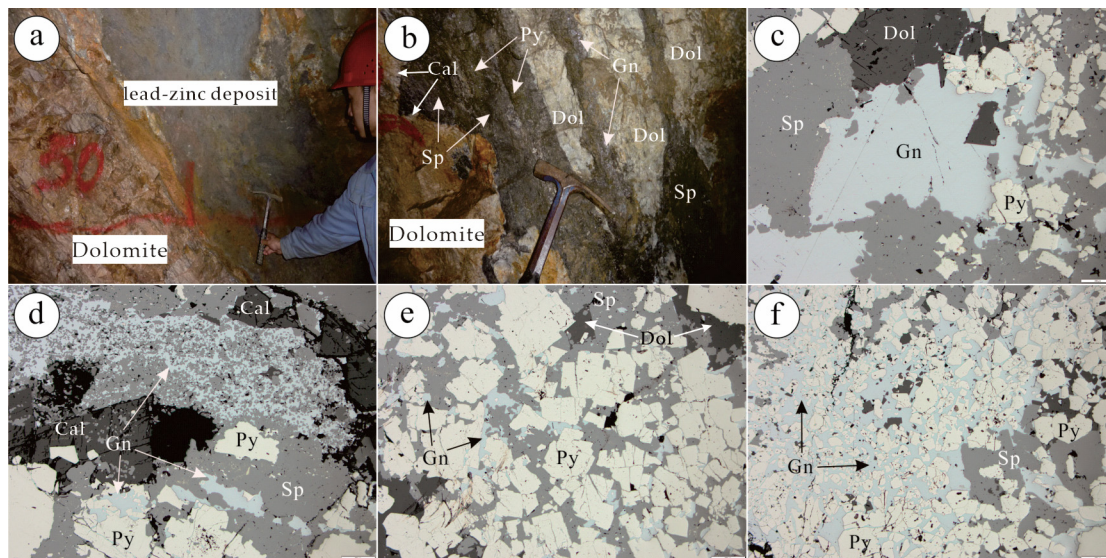
Figure 4. (**a**,**b**) Contact relationship between the wall rocks and the lead–zinc ore; (**c**–**f**) characteristics of the minerals under the microscope; Cal: calcite, Dol: dolomite, Sp: sphalerite, Gn: galena, Py: pyrite.

The gangue minerals were mainly dolomite and calcite. The crystal size of the dolomite in the mining area was 1–5 mm, and some crystals were larger than 5 mm. The crystal structure of the dolomite was granular euhedral or semi-euhedral. In Figure 4c, it can be observed that there were some fragments of pyrite and galena in the dolomite, indicating that the formation time of the dolomite was earlier than that of the metal minerals. The calcite was mainly banded and massive. Figure 4d shows that that calcite was partially replaced by the sphalerite and pyrite, and that there were some pores in the calcite.

3.4. Wall Rock Alteration Characteristics

The wall rock alteration type of the Huize lead–zinc deposit was relatively simple. The hanging wall rock and footwall rock of the orebody were both dolomitized. The footwall alteration of the orebody was more developed, and the hanging wall alteration was slightly or not developed. The dolomitization was widely developed in the middle–upper layer of the Baizuo Fm, but there was less pyritization, carbonation and silicification.

Dolomite alteration: The Lower Carboniferous Baizuo Fm was a light gray–beige, medium-coarse crystalline dolomite and light gray or gray micritic cryptocrystal limestone. Dolomite is mainly distributed in the footwall of ore body, these dolomites have many pores. The mineral composition was primarily dolomite with a content of more than 50%, followed by calcite. The main mineral of the limestone was calcite, with a content of more

than 90%, however it also contained a small amount of dolomite, clay minerals and quartz. The contact boundary between the limestone and the orebody was sharp.

Pyrite replacement: Pyrite often occurs in dolomite outside the orebody or in the fracture zones near the orebody. Larger pyrite crystal has 20 mm in the bottom strata of the middle Carboniferous system, the thickness of pyrite body in some places is 5–6 m. The pyritization is strong in the areas close to the orebody and weak in the areas away from the orebody.

Carbonate alteration: The calcite was mainly developed in the Lower Carboniferous Baizuo Fm, followed by filling in the NW-trending faults. In the ore bodies and fissures, calcite occurs as lumps or veins [34].

4. Sampling and Analytical Methods

4.1. Tunnel Geological Information Record and Sample Collection

The field investigation found that there was a phenomenon of alteration zoning from the orebody to the wall rocks in the Huize lead–zinc deposit. There was silicified dolomite near the orebody (width 5–15 m) and coarse crystalline dolomite with large crystal holes and small crystal holes appeared successively in areas far from the orebody. In order to identify the relationship between the petrophysical properties of the different alteration zones and the orebody location, the tunnel passing through the orebody of stope No. 2 in the 1211 middle section in the Qilinchang lead–zinc deposit was selected as a typical profile for sampling. On the basis of the detailed field geological catalog, the mineralization and alteration characteristics of each alteration zone and their relationship with the orebody location were analyzed. The sampling was carried out at different locations, as shown in Figure 5a.
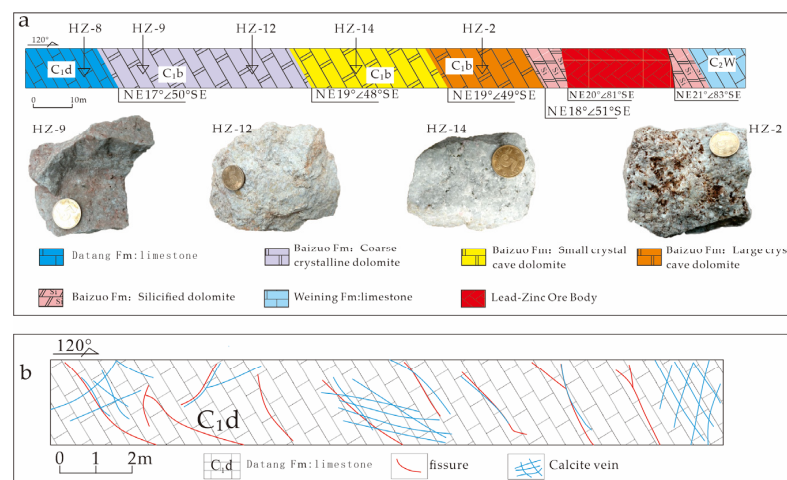
Figure 5. Geological information recording and sampling location of No. 2 stope tunnel in the 1211 middle section of the Qilinchang ore section of the Huize lead–zinc mine: (**a**) sampling location; (**b**) calcite veins and fractures in the Lower Carboniferous Datang Formation limestone.

As shown in Figure 5a, the Lower Carboniferous Datang Formation limestone was 119 m northwest of the orebody, and the color was gray. These limestones were mainly composed of calcite crystals that were less than 1 mm. In addition, in this part of the limestone, the alteration degree was very low, with nearly no dolomitization. This part of the limestone had many cracks and some vein calcite, as shown in Figure 5b. A limestone sample labelled as HZ-8 was collected 122 m to the northwest of the orebody.

The dolomite from the Lower Carboniferous Baizuo Formation, which exhibits segmentation, was located 119 m to the northwest of the position of the orebody. In the 119–70 m range, weakly altered dolomite was identified, and the color was grayish white. The composition was mainly dolomite and calcite, of which about 70% was dolomite. The size of the dolomite crystals were 0.2–2 mm, and some calcite crystals less than 0.2 mm were

filled into the pores between the dolomite crystals. There was no lead–zinc mineralization in this part of the dolomite, but there were scattered pyrite and limonite. The pyrite was mainly euhedral, and the crystal form of the limonite was the same and was formed from the oxidation of the pyrite. The limonite was mainly distributed around the pyrite and dolomite crystals, which dyed the pyrite and dolomite red. There were a few cracks and geodes in this part of the dolomite, and the size of the geodes were 0.3–0.5 mm.

Sample HZ-9 was collected 108 m northwest of the orebody. The sample was gray. The main minerals were dolomite and calcite, and the content of the dolomite was more than 65%. The dolomite crystal size was 1–2 mm, and the calcite crystals were relatively small. This sample had few geodes and cracks. The radii of the geodes were approx. 0.4–0.6 mm. Sample HZ-12 was collected at a position 80 m northwest of the orebody. It was grayish white. The main minerals were dolomite and calcite, and the dolomite content was more than 70%. The size of the dolomite crystals were 1–2 mm, and the calcite crystals could only be seen using a magnifying glass. This sample had more geodes and cracks than HZ-9. The radii of the geodes was approx. 0.4–0.7 mm. At a location 70–35 m to the northwest of the orebody, strongly altered dolomite was identified with many small geodes, and the color was gray white. These dolomites were primarily composed of dolomite and calcite, and the content of the dolomite was more than 75%. The dolomite crystal size was generally larger than 2 mm, and the calcite was mainly veined, which could be seen clearly with a magnifying glass. Some galena and sphalerite were dispersed in this part of the dolomite. Sample HZ-14 was collected 53 m northwest of the orebody and was white. At this sampling location, there were some fine galena, sphalerite and pyrite distributed into the joint surface, cracks and geodes of the dolomite. The radii of the sample geodes were approx. 0.5–1 mm.

In the 35–10 m range to the northwest of the orebody, strongly altered dolomite was discovered with many large geodes. The radii of these geodes were 1.5–6 mm. The surface color of this part of dolomite was gray, and the color of the section after knocking was white. These dolomites were primarily composed of dolomite and calcite, with a dolomite content of more than 75%. The dolomite crystals were larger than 2 mm. Sample HZ-2 was collected at a position 20 m northwest of the orebody, and the dolomite content exceeded 75%. The surface of this sample was gray, and there were more geodes than the other samples. The hole radii of the geodes were also larger than the other samples, approx. 4–6 mm. Red limonite could be seen in these geodes. From 10 m to the northwest of the orebody to the location of the orebody, silicified dolomite of the Lower Carboniferous Baizuo Formation was discovered, with a crystal size of more than 4 mm. This part of the dolomite was grayish white, and there was a small number of geodes. Due to the strong silicification, these dolomites had a relatively high hardness. Near the contact between the dolomite and the orebody, there were some sphalerite, galenite and pyrite veinlets.

The next position was the orebody in this tunnel. The occurrence of this part of the lead–zinc orebody was layered, lenticular and veined, generally distributed into the cracks of the stratum. The main minerals were sphalerite, galena and pyrite. The gangue minerals were calcite, dolomite, barite and quartz. At 6 m to the southeast of the orebody, limestone of the Upper Carboniferous Weining Formation was discovered, which was gray in color. These limestones were mainly composed of calcite (more than 80%). At this location, sphalerite and galena were not seen, but some scattered pyrite was identified.

4.2. Microscopic Characteristics of Samples

The collected samples were made into light sheets, and some phenomena were observed under the microscope. Figure 6a shows the transmitted light micrograph of the HZ-8 sample. No dolomite and metal minerals were observed, and no obvious pores were found. This sample shows the characteristics of the wall rocks before mineralization. Figure 6b shows a transmitted light micrograph of the HZ-9 sample. The mineral composition was mainly pre-mineralization dolomite (HD1), and some limestone fragments can be observed. In addition, the HD1 crystal in Figure 6b was relatively small. Figure 6c

shows the transmitted light micrograph of the HZ-14 sample. It can be observed that some sphalerite was filled in the cracks of HD1. Figure 6d–f shows a microscope photo of the HZ-2 sample at the same position. Among them, Figure 6d shows a reflection light photo, Figure 6e shows a transmitted light photo and Figure 6f shows a cathodoluminescence (CL) photo of this location. It can be observed that the metal minerals replaced part of the HD1 position, and then the metal minerals were replaced by hydrothermal dolomite during the mineralization (HD2) and hydrothermal calcite formed after mineralization (HC). These figures show that the mineralization time was later than that of HD1, but earlier than that of HD2. It can be observed that HD2 replaced part of HD1 in Figure 6g, indicating that the formation of the dolomite had multiple stages. In addition, some large pores can be seen in Figure 6g–I, showing that HD2 was replaced by HC after replacing HD1. Figure 6i shows the phenomenon of HC passing through HD2, indicating that HC was the latest to form. Figure 6j–l shows a photomicrograph of another position of the HZ-2 sample. Figure 6j shows a transmission light photo, Figure 6k shows a CL photo and Figure 6l shows a reflection photo of the pore position in Figure 6k. Some large pores and the dolomite that formed at different times can also be observed in Figure 6j. After amplifying the pores, the pyrite and asphalt can be observed in the pores. This phenomenon indicates that the metal minerals entered the crystal pores of the dolomite during the mineralization. Therefore, we found that the process of the dolomitization had two stages. The process of the dolomitization before the mineralization caused the number of dolomite pores to increase, which increased the porosity and permeability of the dolomite. Then, the metal elements in the hydrothermal fluid entered the pores of the dolomite and filled them, and the porosity of the dolomite was reduced to a certain extent during the mineralization period.
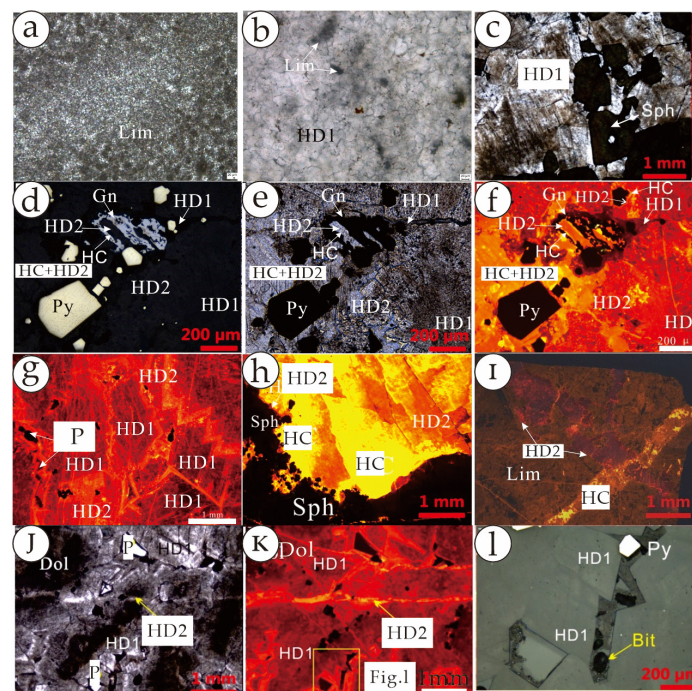
Figure 6. Dolomitization characteristics of the Huize lead–zinc deposit and its relationship to sulfide mineralization. Lim: limestone; (**a**–**c**,**e**,**j**) Transmission light micrograph; (**d**,**j**) reflection photomicrograph; (**f**–**i**,**k**,**l**) cathodoluminescence(CL) photo;Sph: sphalerite; Gn: galena; Py: pyrite; Bit: bitumen; HD1: pre-mineralization dolomite; HD2: hydrothermal dolomite during mineralization; HC: Hydrothermal calcite formed after mineralization; P: pore.

4.3. Analytical Methods

The porosity, permeability and connectivity of the collected samples after processing were measured using micro-scanning (CT) at the Sinopec Wuxi Institute of Petroleum

Geology. The testing instrument was a Zeiss Xradia Versa Micro-CT 520, and the test conditions were an X-ray light source of 60–140 keV and a resolution of 1.00 μm. The exposure time was 3 s, and a 3D reconstruction of the images was completed using the Avizo 9.2 software. The test conditions were as follows: sample sliced with micro-CT; light source voltage, 110 kV; exposure time, 10 s; field of view, 2 × 2 mm; size, 1024 × 1024 pixels; resolution, 1.00 μm.

In this procedure, 900 two-dimensional scanning slice images were obtained for each sample. Next, we applied the reconstruction module technology to reconstruct the 900 two-dimensional grayscale images obtained from the scanning process. Finally, the analysis algorithm in the professional image calculation and processing software was applied to calculate the images obtained from the CT scanning, and the basic pore throat structure parameter information of the sample was obtained, including the pore throat radius, pore volume, specific surface area, etc. The shape, pore distribution, pore connectivity, etc. were displayed using a three-dimensional visualization.

5. Test Results

5.1. Radius of the Pore Throat Channel

For the carbonate rocks, and the radius of the pore throat can directly affect the permeability (pore throat: the interconnected channel between pores [35]). The pore throat radius of sample HZ-9 was in the range of 0.2–2.0 μm but concentrated in the range of 0.2–0.6 μm. This showed that the pore throat radius distribution of this sample was relatively concentrated with a single peak characteristic distribution. The peak characteristics of sample HZ-9 showed that its pore throat radius tended to increase. This showed that the alteration caused some changes in the wall rocks. The pore throat radius of sample HZ-12 was in the range of 0.2–2.0 μm but concentrated in the range of 0.2–0.6 μm, showing that the pore throat radius of this sample was relatively concentrated. It showed a unimodal distribution, but a higher peak appeared in the range greater than 0.2 μm compared to the other samples. This indicates that the tendency of the weak alteration in reforming the pore throats of the wall rocks was to increase the pore throat radius. The pore throat radius of sample HZ-14 was in the range of 0.2–2.0 μm but concentrated in the range of 0.2–0.6 μm. The analysis showed that this was a relatively concentrated distribution with a single peak distribution. In addition, the number of pore throats with a radius > 1 μm in this sample was small, indicating that the throat type in this sample was relatively simple. The pore throat radius of sample HZ-2 was distributed in the range of 0.2–2.0 μm but concentrated in the range of 0.2–0.6 μm. The test data showed that this distribution was relatively concentrated with a unimodal distribution, and there were some throats with a radius greater than 1 μm. The sample had a very small number of pore throats with a radius greater than 2.0 μm, indicating that the pore throat type was relatively complex. Sample HZ-2 showed fewer throats, indicating that it was is strongly squeezed during and after diagenesis, resulting in a poor connectivity of the primary and secondary pores (Table 2 and Figure 7).

Table 2. Test results of the pore throat radius of the carbonate rock samples from the Huize lead–zinc deposit.

Sample Number	HZ-9	HZ-12	HZ-14	HZ-2
Radius (μm)	Frequency	Frequency	Frequency	Frequency
0–0.2	0	0	0	0
0.2–0.4	48	11	154	65
0.4–0.6	19	3	62	45
0.6–0.8	6	1	8	3
0.8–1.0	0	0	1	3
1.0–1.2	2	0	0	0
1.2–1.4	3	0	0	0
1.4–1.6	1	0	0	0
1.6–1.8	0	0	0	0
1.8–2.0	0	0	0	0
>2	4	3	1	7
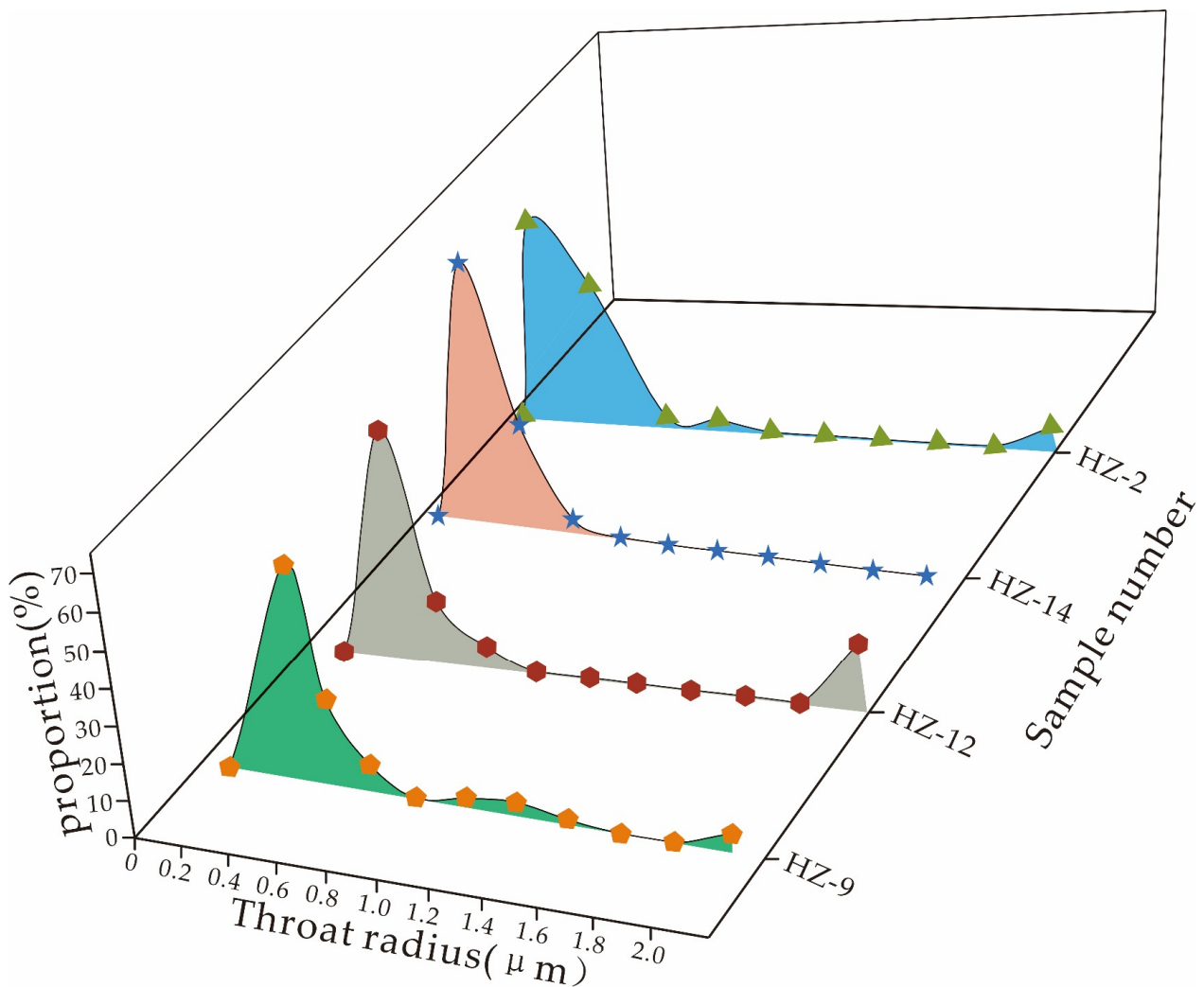
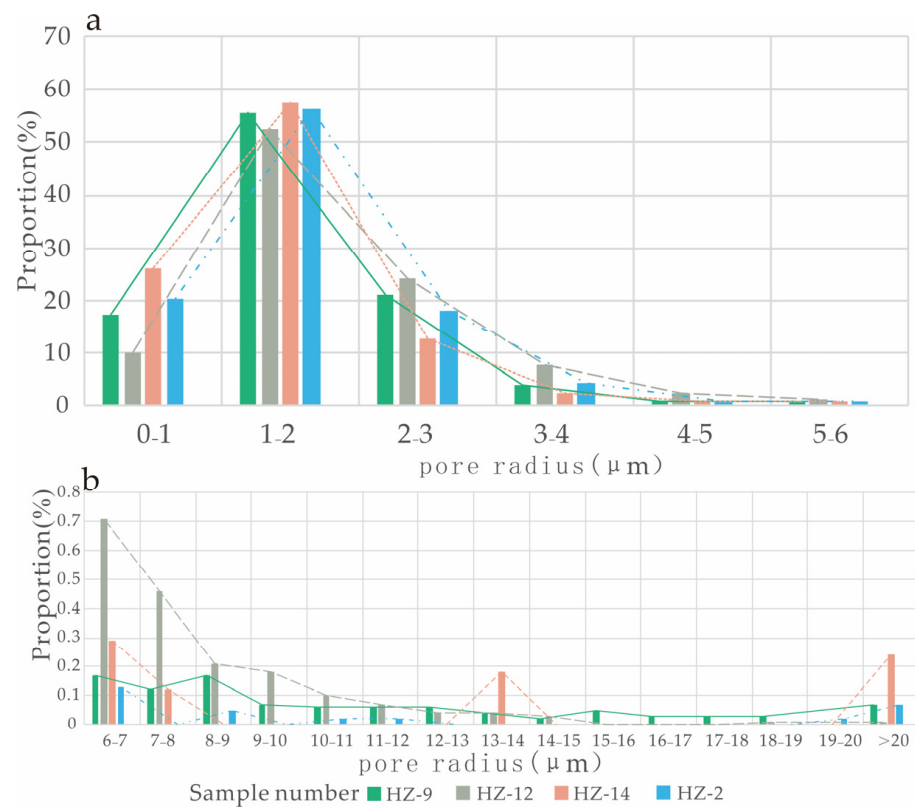**Figure 7.** Ratio of the carbonate pore throat radius in the Huize lead–zinc deposit.

5.2. Pore Radius

The spaces between the mineral particles that comprise a rock are called pores. The pore radius indicates the size of the pores and has a direct effect on the porosity. The pore radius of HZ-9 was between 0.78 and 41.57 μm, among which 94.52% were 0.78–3 μm. The number of pores with a radius greater than 4 μm in this sample was very small, and the pore type was dominated by small pores, with the largest number of small pores among all the samples. The pore radius of sample HZ-12 was between 0.78 and 48.91 μm, among which 96.29% were between 0.78 and 3 μm. The proportion of the pores larger than 4 μm in HZ-12 was very low, and there were only a few pores with a large radius. This indicates that the pore types in this sample were relatively concentrated and were primarily small pores. The pore radius of sample HZ-14 was in the range of 0.89–21.88 μm, concentrated in the range of 1.0–4 μm, and 84.47% of the pores in this sample had a radius between 1 and 4 μm. The proportion of the pores with a radius greater than 4 μm in HZ-14 was higher than the other samples, and there were more large pores, indicating that the pore type in this sample was relatively complex. The pore radius of sample HZ-2 was in the range of 0.78–20 μm, concentrated in the range of 0.78–3 μm, and 94.02% of the pores had a radius of 0.78–3 μm. The proportion of the pores with radius larger than 4 μm in HZ-2 was very low. Although this sample had some large pores, the number was small. This shows that the pore types in this sample were relatively concentrated and were primarily small pores.

The number of pores with a radius larger than 20 μm in HZ-2 was the largest among all the samples (Table 3 and Figure 8).

Table 3. Test results of the pore radius of the carbonate rock samples in the Huize lead–zinc deposit.

Sample Number	HZ-9	HZ-12	HZ-14	HZ-2
Radius (μm)	Frequency	Frequency	Frequency	Frequency
0–1	1245	443	1515	1879
1–2	3412	976	8052	5977
2–3	1084	216	3692	2275
3–4	249	38	1202	418
4–5	50	5	381	86
5–6	16	6	200	36
6–7	8	5	109	18
7–8	0	2	70	13
8–9	3	0	32	18
9–10	0	0	28	8
10–11	1	0	15	7
11–12	1	0	11	6
12–13	0	0	6	6
13–14	0	3	6	4
14–15	0	0	5	2
15–16	0	0	0	5
16–17	0	0	0	3
17–18	0	0	0	3
18–19	0	0	1	3
19–20	1	0	0	0
>20	4	4	2	8

Figure 8. Pore radius ratio of the carbonate rock samples in the Huize lead–zinc deposit. (**a**) Radius 0–6 μm Histogram of the proportion of pores to the total number of pores; (**b**) Radius 6–20 μm and more than 20μm Histogram of the proportion of pores to the total number of pores.

5.3. Pore Volume

The pore volume of sample HZ-9 was in the range of $1–10^6$ μm^3, concentrated in the range $10–10^2$ μm^3. Similar to HZ-12, HZ-9 had some pores larger than 10^5 μm^3, but the number was small. The pore volume of HZ-12 was in the range of $1–10^6$ μm^3, concentrated in the range $10–10^2$ μm^3. The proportion of the pores in HZ-12 between 10^2 and 10^3 μm^3 was 3.2%, which was lower than the other samples in the same interval. The pore volume of sample HZ-14 was in the range of $1–10^5$ μm^3, concentrated in the range $10–10^3$ μm^3. The pore volume of HZ-14 between 10^2 and 10^3 μm^3 was 6.2%, which was higher than the other samples in the same range. The pore volume of sample HZ-2 sample was in the range of $1–10^5$ μm^3 and concentrated in the range of $1–10^2$ μm^3. The proportion of the pore volume greater than 10^4 μm^3 in HZ-2 was 0.26%, which was higher than the other samples (Table 4 and Figure 9).

Table 4. Test results of the pore volume of the carbonate rock samples in the Huize lead–zinc deposit.

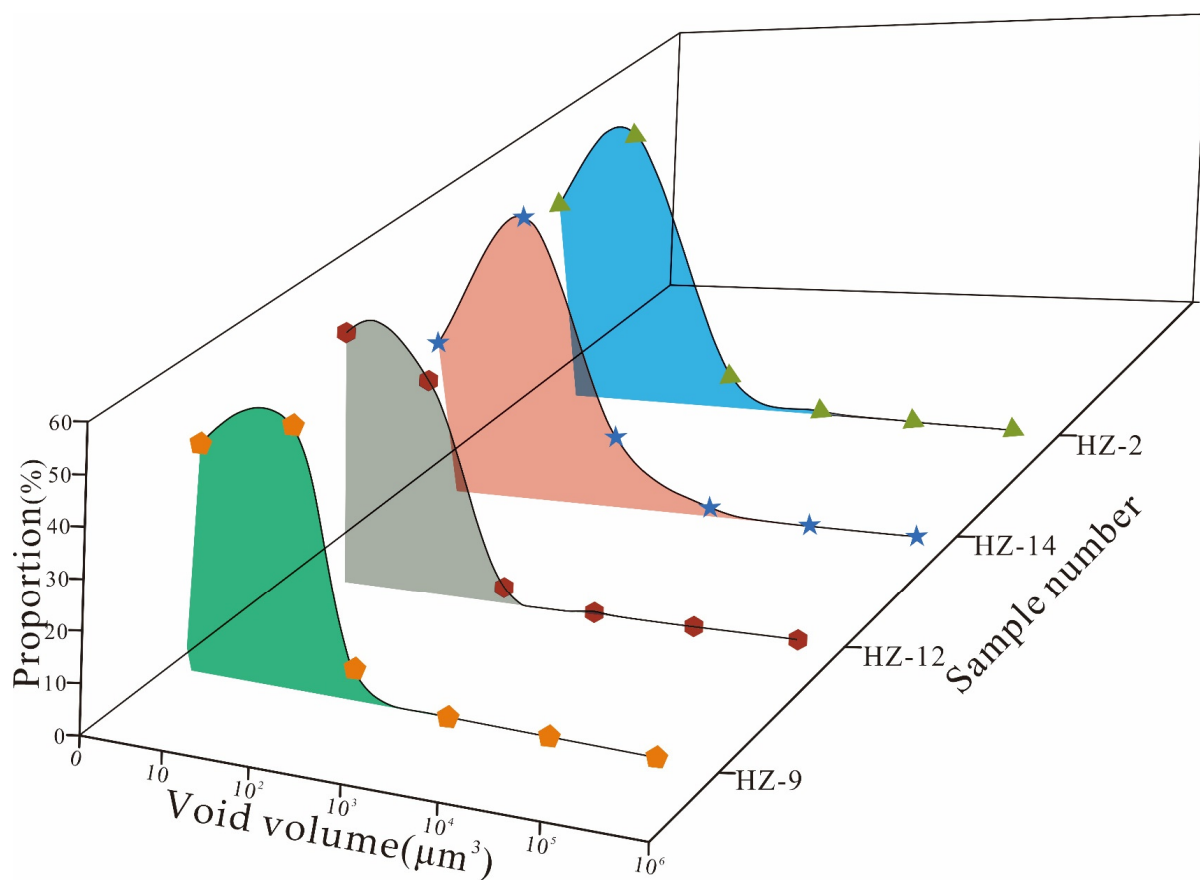| Sample Number	HZ-9	HZ-12	HZ-14	HZ-2
Volume (μm^3)	Frequency	Frequency	Frequency	Frequency
0–10	2694	890	4560	4236
$10–10^2$	3012	740	8436	5772
$10^2–10^3$	352	55	2071	668
$10^3–10^4$	11	7	250	71
$10^4–10^5$	1	2	10	28
$10^5–10^6$	4	4	0	0

Figure 9. Pore volume ratio of the carbonate rock samples in the Huize lead–zinc deposit.

5.4. Pore Surface Area

The pore surface area of sample HZ-9 was between 1 and 10^5 μm^2, concentrated between 10 and 10^2 μm^2. The pore surface area of sample HZ-12 was between 1 and 10^5 μm^2, concentrated between 10 and 10^2 μm^2. In this sample, 4.89% of the pore surface area was between 10^2 and 10^3 μm^2, which was lower than the other samples. However, 0.29% of the pore surface area of this sample was 10^3–10^4 μm^2, higher than the other samples. Further, 94.58% of sample HZ-12 had a pore surface area less than 10 μm^2, which was the highest among all the samples. The pore surface area of sample HZ-14 was between 1 and 10^5 μm^2, concentrated between 10 and 10^3 μm^2. In this sample, 94.14% of the pore surface area was between 10 and 10^3 μm^2, which was higher than the other samples. The pore surface area of sample HZ-2 was between 1 and 10^5 μm^2, concentrated between 10 and 10^3 μm^2. In this sample, 77.25% of the pores had a surface area of 10–10^2 μm^2, slightly higher than the other samples (Table 5 and Figure 10).

Table 5. Test results of the pore surface area of the carbonate rock samples in the Huize lead–zinc deposit.

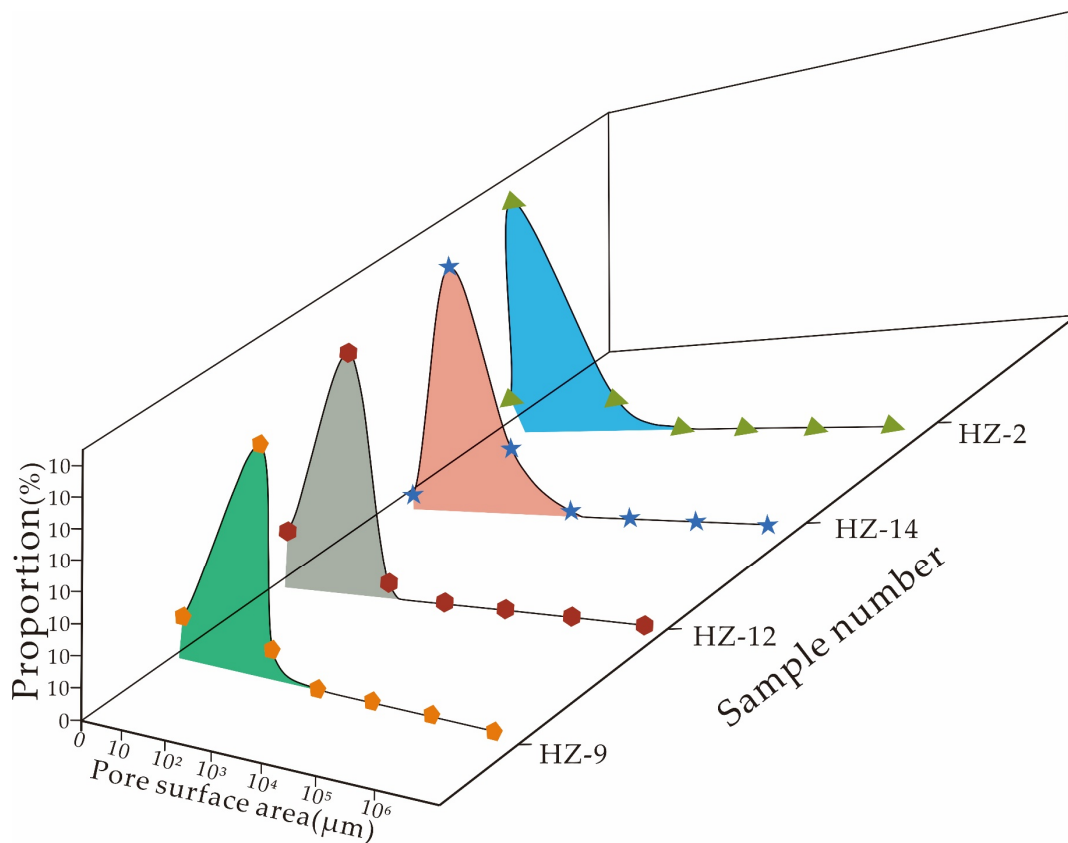| Sample Number	HZ-9	HZ-12	HZ-14	HZ-2
Area (μm^2)	Frequency	Frequency	Frequency	Frequency
0–10	857	315	687	1244
10–10^2	4633	1291	11,481	8324
10^2–10^3	566	83	2954	1115
10^3–10^4	14	5	202	78
10^4–10^5	3	4	3	14
10^5–10^6	1	0	0	0

Figure 10. Pore surface area ratio of the carbonate rock samples in the Huize lead–zinc deposit.

5.5. Face Rate

The face porosity is the ratio of the pore area to the rock section area as seen under a microscope. The porosity of a rock can be calculated using the face rate of multiple slices, and this process was automatically completed by the computer. Each sample was sliced 299 times and scanned using CT to obtain the face rate for each slice. The face rates of the samples are shown in Figure 11, and the porosity of the samples was calculated from the face rate of all the sections (Table 6).
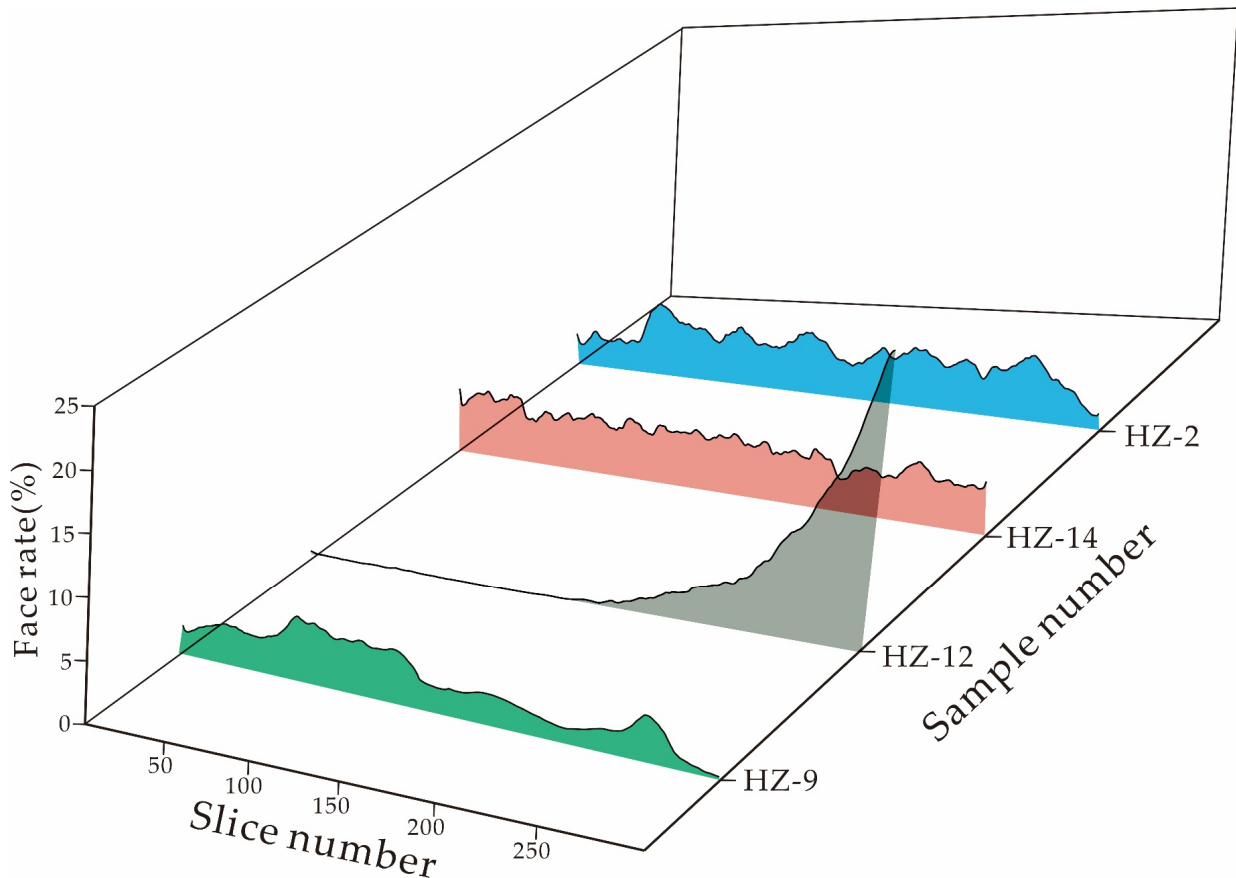

Figure 11. Face rate variation of the carbonate rock samples in the Huize lead–zinc deposit.

Table 6. Pore throat structure parameters of the carbonate rock samples in the Huize lead–zinc deposit.

Sample Number	Average Pore Radius (µm)	Average Pore Throat Radius (µm)	Average Pore Volume (µm³)	Average Specific Surface Area (µm²)	Average Pore Throat Length (µm)	CT Porosity (%)
HZ-9	1.65	0.077	179.87	91.01	29.57	2.81
HZ-12	1.60	1.02	857.55	159.76	39.95	2.76
HZ-14	2.05	0.38	110.86	107.55	13.57	3.99
HZ-2	1.77	0.55	120.46	92.11	16.83	3.35

The face rate of sample HZ-9 was between 0.25 and 5.48%. The face rate of sample HZ-12 was between 0.01 and 22.31%. The variation range of the porosity of this sample was the largest, indicating that the face rate was extremely heterogeneous, and the degree of the pore change was large. The face rate of sample HZ-14 was between 2.40 and 5.31%. The face rate of this sample changed minimally, indicating that the heterogeneity of the sample was small, and the degree of the pore change was low. The face rate of sample HZ-2 was between 0.98 and 5.50%. The face rate of HZ-9 and HZ-2 also changed greatly in the

different sections, indicating that the two samples had a large heterogeneity and a large pore change.

The calculations show that the porosity of sample HZ-12 was the lowest (Table 6), but the face rate varied greatly (Figure 11). Although the porosity of sample HZ-9 was not high, the face rate was relatively uniform (Figure 11). This shows that the alteration far from the orebody had a great influence on the porosity of the wall rocks, promoting the production of larger pores in the wall rocks. However, the wall rocks close to the orebody became homogeneous again due to the recrystallization and strong mineralization. The porosity of the HZ-14 and HZ-2 samples were relatively uniform, showing the characteristics of a uniform pore distribution in the wall rocks near the orebody. The other statistical data show that the average pore radius increased with the decreasing distance to the orebody. The average pore volume decreased with the decreasing distance to the orebody. The variation characteristics of the average porosity increased with the decreasing distance to the orebody. The result of the porosity increase conforms to the law of the dolomitization process. The changed rules of the pore radius and the pore volume indicate that there should be changes in the number of pores used in this process. In terms of the test data of the pore throats, the average pore throat radius and the average pore throat length became smaller with the decreasing distance to the orebody. This result shows that the connectivity between the pores became weak.

6. Discussion

6.1. Variation in the Porosity with the Decreasing Distance from Ore Bodies

The micro-CT scan of sample HZ-9 is shown in Figure 12, in which the black part represents the pores, and the gray part represents the rock matrix.
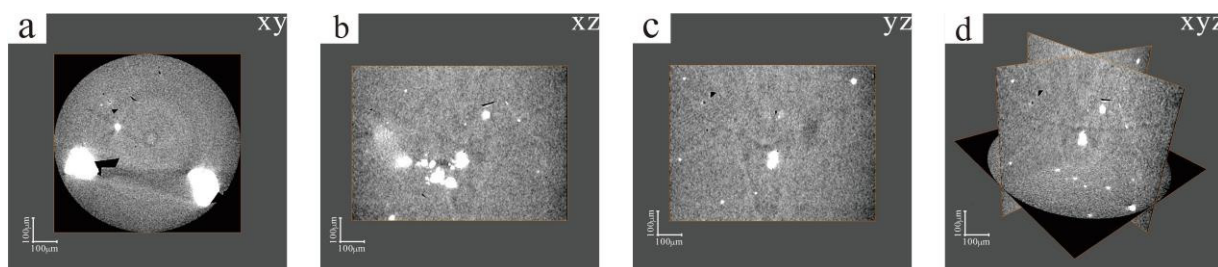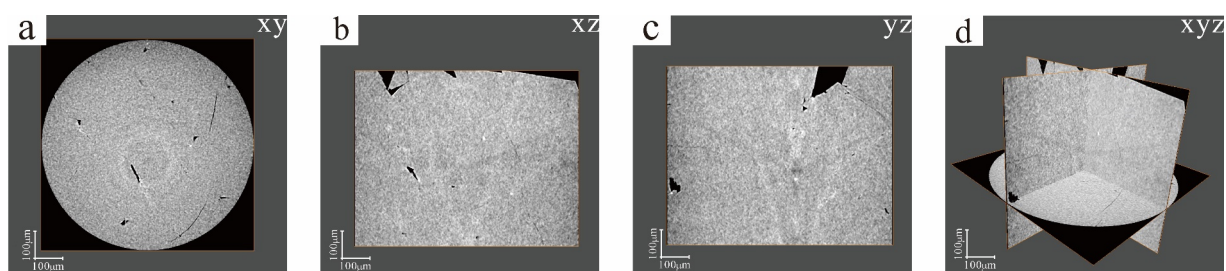

Figure 12. Micro-CT slice image of sample HZ-9 in the Huize lead–zinc deposit.(**a**) Sample xy section Micro-CT scan image; (**b**) Sample xz section Micro-CT scan image; (**c**) Sample yz section Micro-CT scan image; (**d**) Micro-CT scanning mosaic image of sample xyz section.

The skeleton extraction was performed on the pore throat network of the slice using the application software, and its spatial distribution model is shown in Figure 13a–c. Sample HZ-9 was compared with the other three samples and was found to have less pore development, relatively more throats and a better connectivity between the pores. The lowest gray part (pore and pore throat) in the gray image was extracted and segmented using threshold segmentation to separate the pore and the pore throat from the rock matrix. The Avizo 9.2 software was used to segment and extract the distribution positions, distribution forms and distribution of the pores and throat networks in the sample space, and a three-dimensional display was constructed. The results are shown in Figure 13d–f. By analyzing the three-dimensional diagram, we can conclude that the degree of the pore development of HZ-9 was low. The pores of this sample were mainly macropores, and there were multiple small pores. The porosity of this sample was calculated to be 2.81% (Table 6), which is in the ultra-low range. Based on the separate extraction of the pores from the matrix and particles, the separate object technique was used to analyze the spatial connectivity distribution characteristics of the pores, as shown in Figure 13g–i. Figure 13 shows that sample HZ-9 had a low degree of pore development, with large pores occupying a larger space, in addition to some small pores.
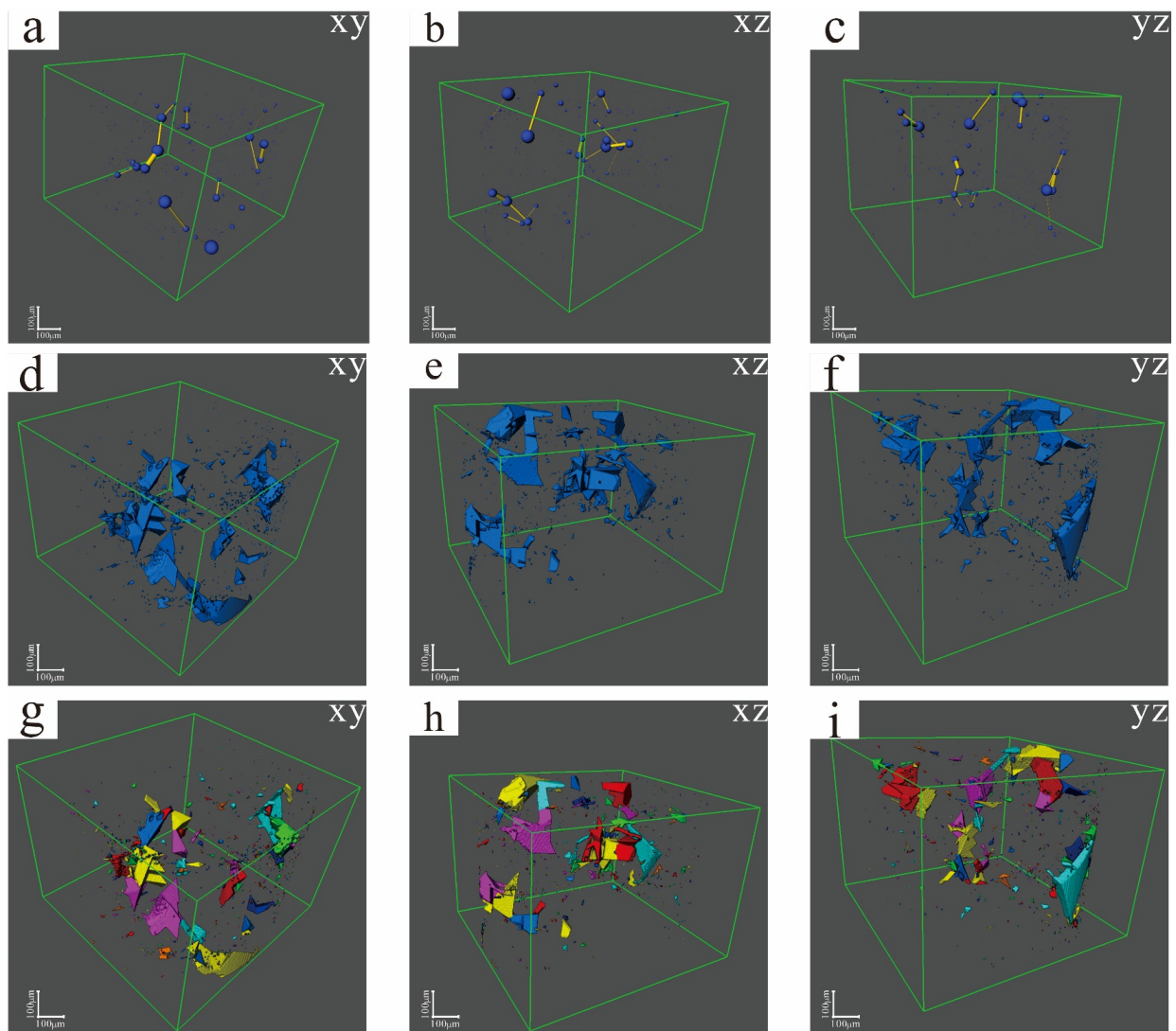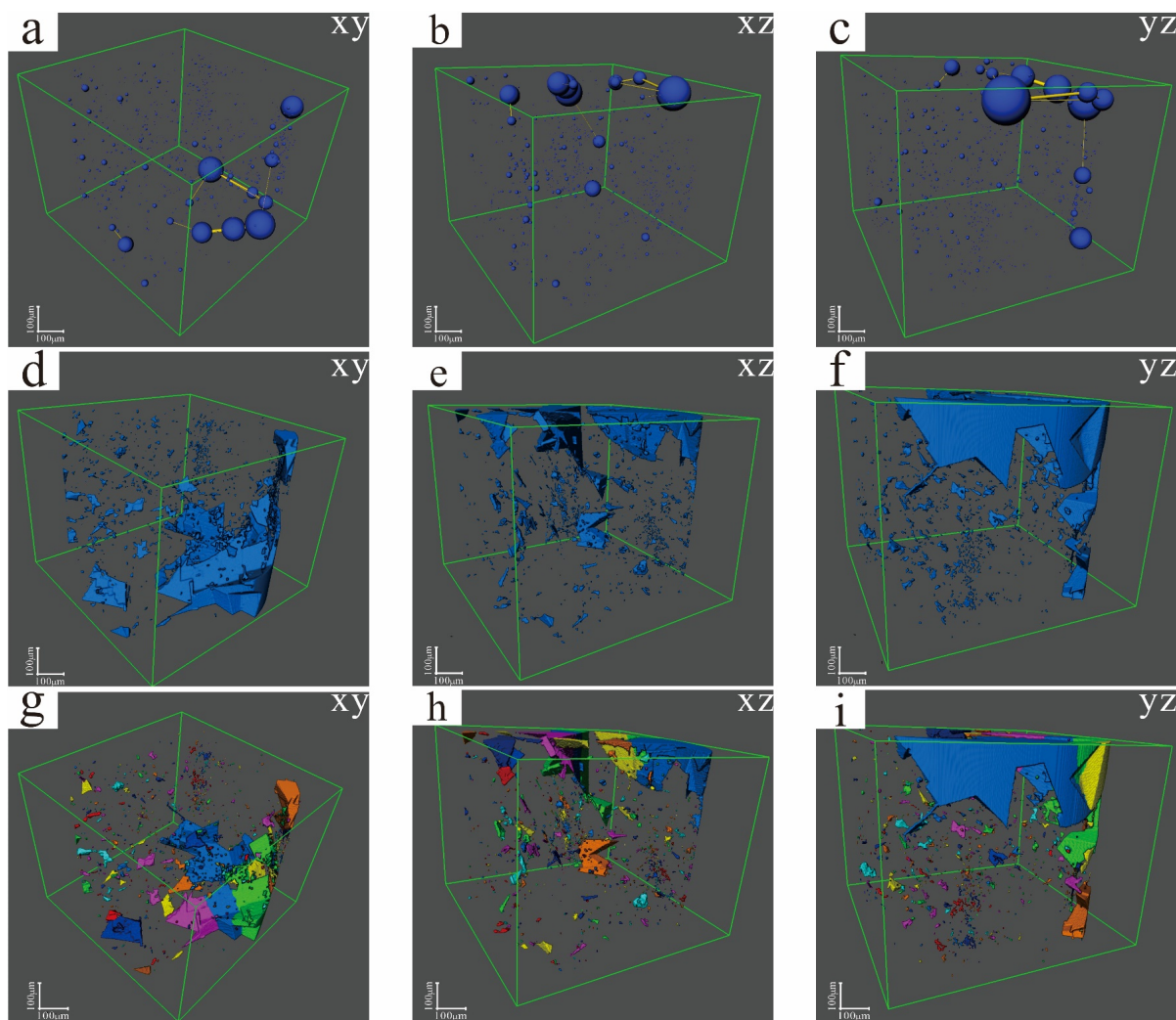
Figure 13. Pore and pore throat structure imaging of sample HZ-9: (**a**–**c**) the blue spheres represent the pores, and the yellow lines represent the pore throats; (**d**–**f**) blue represents the spatial position of the pores and pore throats; (**g**–**i**) the pores with similar colors in adjacent regions are connected.

The micro-CT scan of sample HZ-12 is shown in Figure 14, in which the black part represents the pores, and the gray part represents the rock matrix. Although HZ-12 had fewer pores, there were some dispersed macropores.

Figure 14. Micro-CT slice image of sample HZ-12 in the Huize lead–zinc deposit.(**a**) Sample xy section Micro-CT scan image; (**b**) Sample xz section Micro-CT scan image; (**c**) Sample yz section Micro-CT scan image; (**d**) Micro-CT scanning mosaic image of sample xyz section.

The skeleton extraction was performed on the pore throat network of the slice using the application software, and its spatial distribution model is shown in Figure 15a–c. Sample HZ-12 had many large pores with a good connectivity and generally isolated small pores. The lowest gray part (pore and pore throat) in the gray image was extracted and segmented using threshold segmentation to separate the pore and the pore throat from the rock matrix. The Avizo 9.2 software was used to segment and extract the distribution positions, distribution forms and distribution of the pores and throat networks in the sample space, and a three-dimensional display was constructed. The results are shown in Figure 15d–f. The porosity of this sample was calculated to be 2.76% (Table 6), which is in the ultra-low range. Based on the separate extraction of the pores from the matrix and particles, the separate object technique was used to analyze the spatial connectivity distribution characteristics of the pores, as shown in Figure 15g–i. Figure 15 shows that the pore connectivity of HZ-12 was poor. Some large pores were interconnected and the small pores were poorly connected.

Figure 15. Pore and pore throat structure imaging of sample HZ-12: (**a**–**c**) the blue spheres represent the pores, and the yellow lines represent the pore throats; (**d**–**f**) blue represents the spatial position of the pores and pore throats; (**g**–**i**) the pores with similar colors in adjacent regions are connected.

The micro-CT scan of sample HZ-14 is shown in Figure 16, where the black part represents the pores, and the gray part represents the rock matrix. The pores of HZ-14 were generally small and dispersed.
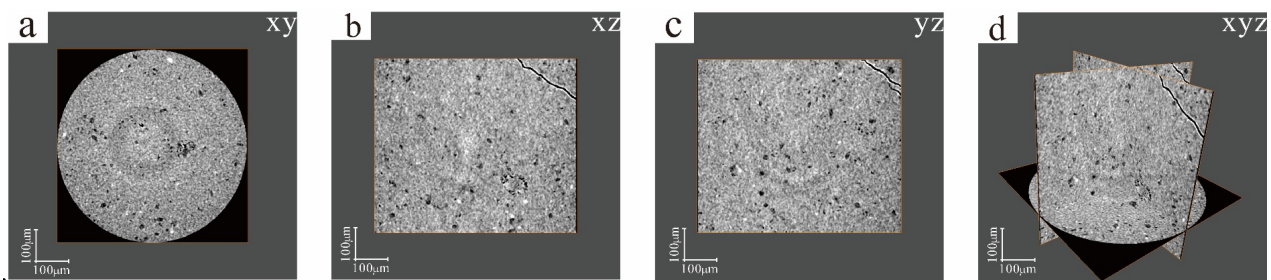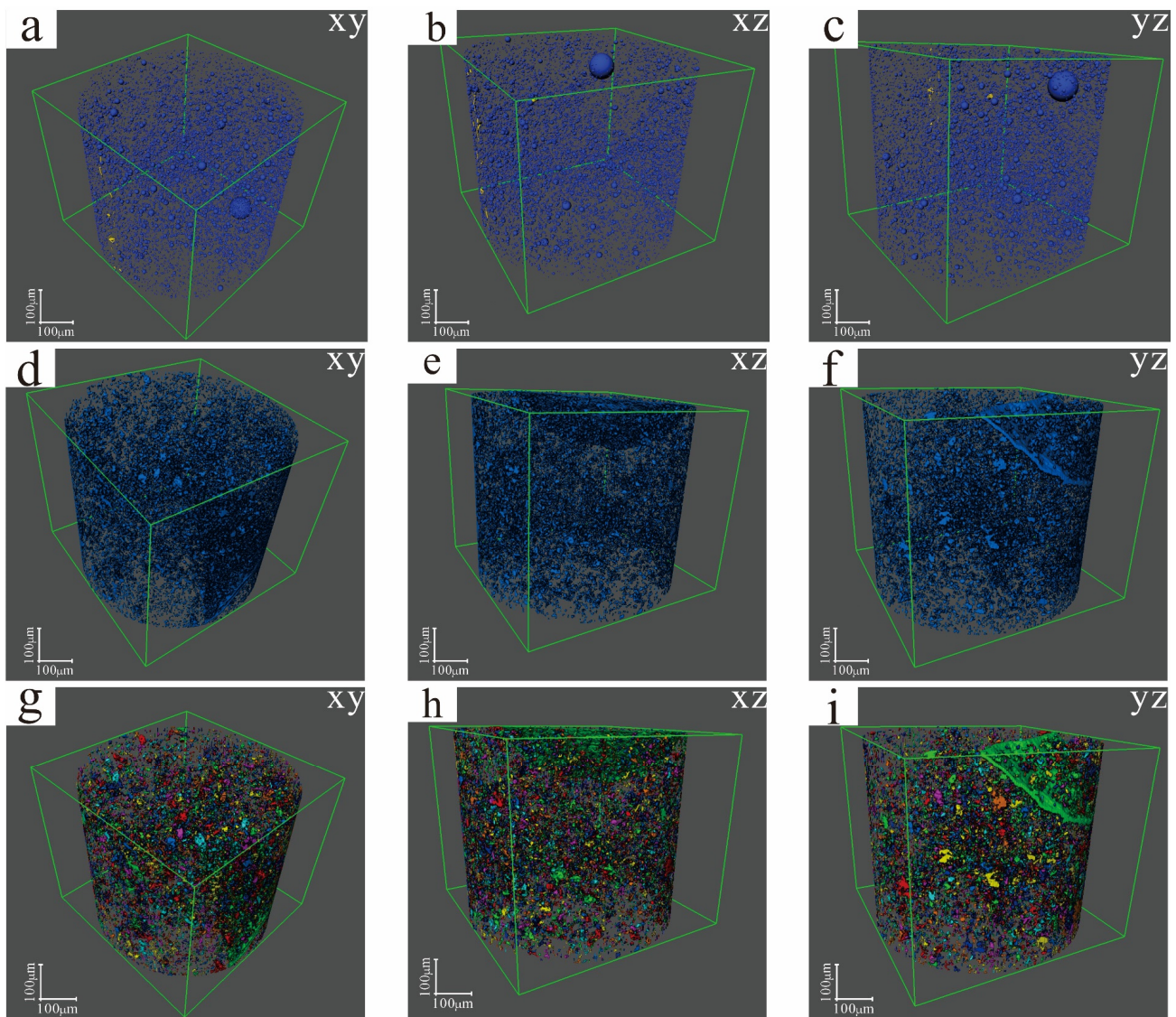
Figure 16. Micro-CT slice image of sample HZ-14 in the Huize lead–zinc deposit. (**a**) Sample xy section Micro-CT scan image; (**b**) Sample xz section Micro-CT scan image; (**c**) Sample yz section Micro-CT scan image; (**d**) Micro-CT scanning mosaic image of sample xyz section.

The skeleton extraction was performed on the pore throat network of the slice using the application software, and its spatial distribution model is shown in Figure 17a–c. The number of small pores in sample HZ-14 was particularly large, but the number of pore throats between the pores was small and the pore connectivity was poor. The lowest gray part (pore and pore throat) in the gray image was extracted and segmented using the threshold segmentation technique to separate the pore and the pore throat from the rock matrix. The Avizo 9.2 software was used to segment and extract the distribution positions, distribution forms and distribution of the pores and throat networks in the sample space, and a three-dimensional display was constructed. As shown in Figure 17d–f, sample HZ-14 had a relatively high degree of pore development and dense pores. The porosity of this sample was calculated to be 3.99% (Table 6), which is in the ultra-low range. Based on the separate extraction of the pores from the matrix and particles, the separate object technique was used to analyze the spatial connectivity distribution characteristics of the pores, as shown in Figure 17g–i. Figure 17 shows that the pore connectivity of HZ-14 was relatively poor, and most pores showed an isolated distribution.

The micro-CT scan of sample HZ-2 is shown in Figure 18, in which the black part represents the pores, and the gray part represents the rock matrix. It can be observed that HZ-2 mainly had scattered small pores.

The skeleton extraction was performed on the pore throat network of the slice using the application software, and its spatial distribution model is shown in Figure 19a–c. The lowest gray part (pore and pore throat) in the gray image was extracted and segmented using the threshold segmentation technique to separate the pore and the pore throat from the rock matrix. The Avizo 9.2 software was used to segment and extract the distribution positions, distribution forms and distribution of the pores and throat networks in the sample space, and a three-dimensional display was constructed. As shown in Figure 19d–f, the degree of the pore development of HZ-2 was relatively low. There were some superimposed large pores also in addition to a large number of small pores. The porosity of this sample was calculated to be 3.35% (Table 6), which is in the ultra-low range. Based on the separate extraction of the pores from the matrix and particles, the separate object technique was used to analyze the spatial connectivity distribution characteristics of the pores, as shown in Figure 19g–i. Comparing the results of the four samples, the number of pores in the HZ-9 and HZ-12 samples was relatively small. However, there were many pore throat connections between these pores (Figures 13a–c and 15a–c). Therefore, the pore connectivity of the HZ-9 and HZ-12 samples were relatively better (Figures 13g–i and 15g–i). There were many pores in the HZ-14 and HZ-2 samples. However, there were few pore throats between these pores (Figures 17a–c and 19a–c). So, the pore connectivity of the HZ-14 sample, and the HZ-2 sample were relatively weak (Figures 17g–i and 19g–i).

Figure 17. Pore and pore throat structure imaging of sample HZ-14: (**a**–**c**) the blue spheres represent the pores, and the yellow lines represent the pore throats; (**d**–**f**) blue represents the spatial position of the pores and pore throats; (**g**–**i**) the pores with similar colors in adjacent regions are connected.
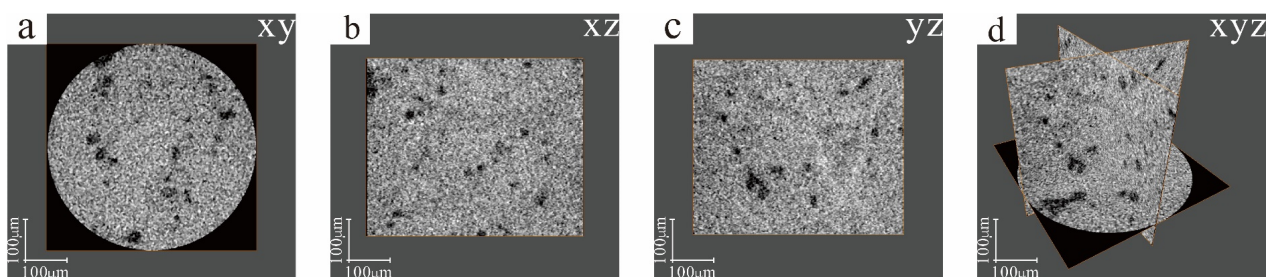
Figure 18. Micro-CT slice image of sample HZ-2 in the Huize lead–zinc deposit. (**a**) Sample xy section Micro-CT scan image; (**b**) Sample xz section Micro-CT scan image; (**c**) Sample yz section Micro-CT scan image; (**d**) Micro-CT scanning mosaic image of sample xyz section.
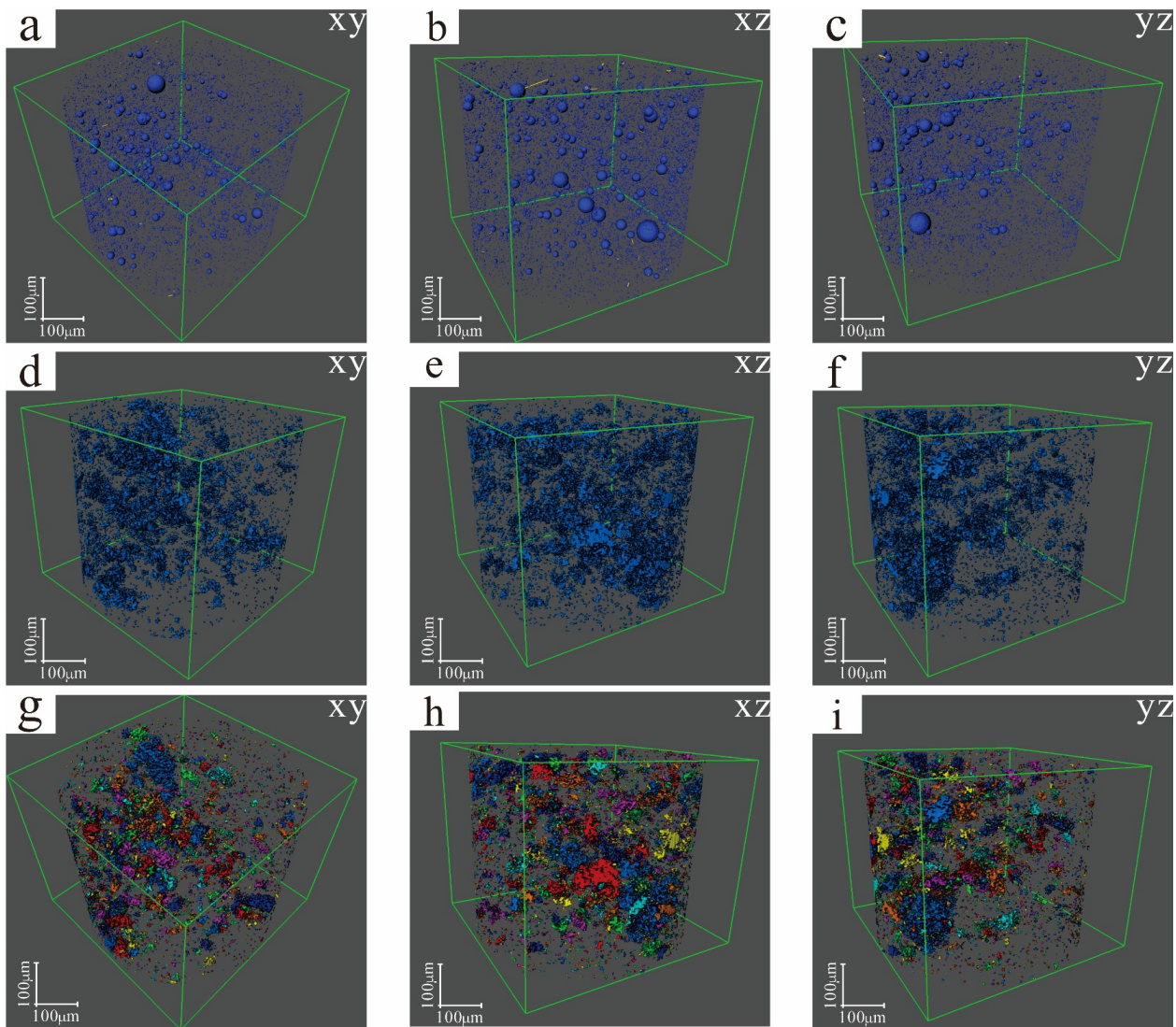
Figure 19. Pore and pore throat structure imaging of sample HZ-2: (**a**–**c**) the blue spheres represent the pores, and yellow lines represent the pore throats; (**d**–**f**) blue represents the spatial position of the pores and pore throats; (**g**–**i**) the pores with similar colors in adjacent regions are connected.

6.2. Relationship between the Alteration, Porosity and Ore Location

Some scholars believe that the coarse-grained dolomite of Baizuo Fm, Zaige Fm and Dengying Fm that developed throughout the Huize lead–zinc deposit was formed by the combined action of tectonic and hydrothermal alteration. The fine-grained dolomite, dolomite limestone and limestone in the deposit after alteration, became coarse-grained dolomite. Reticulated dolomite limestone is a transitional type of rock between dolomite and limestone formed through incomplete alteration [36]. From the test results, the wall rocks around the Huize lead–zinc mine were positioned far from the orebody to near the orebody. As the alteration strengthened, the porosity of the dolomite increased. The dolomite far from the orebody had fewer pores, a larger pore volume variation, a larger throat length and better connectivity between the pore throats. Toward the position close to the orebody, the dolomite samples had more pores and fewer pore throats, with only a few independent small pores, except for geodes or fissures. (Figures 16 and 18). This shows that near the orebody, after the hydrothermal fluids have penetrated the wall rocks on both sides, the fluid reacted strongly with the wall rocks. In this process, a large number of calcite, dolomite and other minerals gradually precipitated and occupied the gaps between

the dolomite particles. As a result, the connectivity of the dolomite near the orebody became poor.

The connectivity of the dolomite is primarily related to the pores and throats, which determine the permeability [22]. The permeability is a key geological parameter and a major controlling factor for the fluid flow and heat transfer [37], so variations in the permeability can indicate the presence of mineralization. The permeability is largely related to the size and type of the pores, the shape and size of the pore throats and the special surface of the pores [38]. Therefore, the study of the characteristics of the carbonate pores and throats can reflect the characteristics of the permeability to some extent. Dolomite sample HZ-9, far from the orebody, was compared with samples HZ-12 and HZ-14, closer to the orebody. Its porosity was small, there were some overlapping large pores and the pore connectivity was good (Figures 13, 15 and 17). Dolomite sample HZ-2, closest to the orebody, had a large number of small pores. These small pores were isolated from each other, with less pore throat development and a poor connectivity between the pores. This difference may be related to the alteration and recrystallization of the dolomite caused by mineralization, resulting in the formation of geodes and an increased number of pores, after which the hydrothermal fluids occupied the pores and throats. The end result is that the closer to the orebody, the smaller the pore radius of the sample, the fewer the throats and the worse the pore connectivity.

7. Conclusions

(1)   As the surrounding rock decreases in distance to the orebody, the porosity tends to increase. The CT porosity of the two dolomite samples far away from the orebody were 2.76%–2.81%. The 3D image shows that the number of dolomite pores at this location was relatively small. The CT porosity of the two dolomite samples near the orebody were 3.35%–3.99%. It can be seen from the 3D images that the number of pores in the two samples was large. It can be found that the porosity of the dolomite increased with a decreasing distance to the orebody. This increase was related to the increase in the number of pores. In the microscopic photos, we observed that there were some metal minerals filling the sample pores near the orebody. This indicates that the metal minerals enter and fill the dolomite pores during the mineralization.

(2)   The average pore throat radii of the two samples far away from the orebody were 0.77 µm and 1.02 µm, and the average pore throat lengths were 29.57 µm and 39.95 µm. From the 3D image, it can be observed that the number of pore throats in these two samples was large, and many of the pores were interconnected. The average pore throat radii for the two samples near the orebody were 0.38 µm and 0.55 µm, and the average pore throat lengths were 13.57 µm and 16.83 µm. Compared to the samples far away from the orebody, their pore throat radii and pore throat lengths were smaller, which means that the samples near the orebody had low permeability and poor connectivity between the pores. It can also be observed from the 3D image that the number of sample pore throats near the orebody was small and the pores were isolated. This phenomenon indicates that the shorter the distance from the orebody, the worse the permeability of the dolomite. Based on the combined analysis of the microscopic photos and the 3D images, the author believes that the surrounding rock near the orebody underwent two stages of dolomitization due to the influence of hydrothermal activity. In this process, the number of pores in the surrounding rock increased, so the porosity of the dolomite increased. However, the hydrothermal minerals (Sph, Gn, Py) filled a part of the pores and pore throats, resulting in a smaller pore radius and pore throat radius and a smaller pore volume and pore throat length. Therefore, the connectivity between the pores of the samples near the orebody was worse than the samples far away from the orebody. The final result is that, with a decreasing distance to the orebody, the porosity of the dolomite increases and the permeability decreases. According to the above test results and analysis, the author believes that the gray-white coarse-porous crystalline dolomite developed in the Huize lead–zinc mine

area can be used as one of the main indicators for future prospecting. The direction of the dolomite porosity increase and the permeability decrease may represent the direction of the orebody.

References

1. Zhang, C.Q.; Yu, J.J.; Mao, J.; Rui, Z.Y. Advances in the study of Mississippi valley-type deposits. *Miner. Depos.* **2009**, *28*, 195–210.
2. Mao, J.; Li, X.; Li, H.; Qu, X.; Zhang, C.; Xue, C.; Wang, Z.; Yu, J.J.; Zhang, Z.; Feng, C.; et al. Types and characteristics of endogenetic metallic deposits in orogenic belts in China and their metallogenic processes. *Acta Geol. Sin.* **2005**, *79*, 342–371.
3. Zhen, S.; Zhu, X.; Li, Y. A tentative discussion on Mississippi valley-type deposits. *Miner. Depos.* **2013**, *32*, 367–379.
4. Davis, J.H. Genesis of the Southeast Missouri lead deposits. *Econ. Geol.* **1977**, *72*, 443–450. [CrossRef]
5. Davies, G.; Smith, L. Structurally controlled hydrothermal dolomite reservoir facies: An overview. *AAPG Bull.* **2006**, *90*, 1641–1690. [CrossRef]
6. Machel, H.G.; Lonnee, J. Hydrothermal dolomite—A product of poor definition and imagination. *Sediment. Geol.* **2002**, *152*, 163–171. [CrossRef]
7. Huang, S.J. *Diagenesis of Carbonate Rocks*; Geological Publishing House: Beijing, China, 2010.
8. Zhang, Z.; Li, C.; Tu, G.; Xia, B.; Wei, Z. Geotectonic evolution background and ore-forming process of Pb-Zn deposits in Chuan-Dian-Qian area of Southwest China. *Geotecton. Metallog.* **2006**, *30*, 343–354.
9. Han, R.; Wang, F.; Hu, Y.; Wang, X.; Ren, T.; Qiu, W.; Zhong, K. Metallogenic tectonic dynamics and chronology constrains on the huize-type (HZT) germanium-rich silver-zinc-lead deposits. *Geotecton. Metallog.* **2014**, *38*, 758–771.
10. Zhang, C.Q. *Distribution, Characteristics and Genesis of Mississippi Valley-Type Lead-Zinc Deposits in the Triangle Area of Sichuan-Yunnan-Guizhou Provinces*; China University of Geosciences: Beijing, China, 2005.
11. Zhang, C.Q. *The Genetic Model of Mississippi Valley-Type Deposits in the Boundary Area of Sichuan, Yunnan and Guizhou Provinces*; Chinese Academy of Geological Sciences: Beijing, China, 2008.
12. Wang, J. Localization Rules of Large Pb-Zn Deposits in the Southwestern Margin of the Upper-Middle Yangtze Block. Ph.D. Thesis, China University of Geosciences, Beijing, China, 2018.
13. Wu, J.; Li, G.; Li, Y.; Wei, J.; Wang, H.; Li, P. Chronology research progress of the MVT lead-zinc deposit in the border area of Sichuan-Yunnan-Guizhou and the background of metallogenic tectonics. *Geol. Sci. Technol. Info.* **2019**, *38*, 134–144.
14. Kong, Z.; Wu, Y.; Zhang, F.; Zhang, C.; Meng, X. Sources of hydrothermal fluids of typical Pb-Zn deposits in the Sichuan-Yunnan-Guizhou metallogenic province: Constraints from the S-Pb isotopic compositions. *Earth Sci. Front.* **2018**, *25*, 125–137.
15. Kong, Z.; Zhang, B.; Wu, Y.; Zhang, C.; Liu, Y.; Zhang, F.; Li, Y. Structural control and metallogenic mechanism of the Daliangzi Ge-rich Pb-Zn deposit in Sichuan province, China. *Earth Sci. Front.* **2022**, *29*, 143.
16. Wu, Y. The Age and Ore-Forming Process of MVT Deposits in the Boundary Area of Sichuan-Yunnan-Guizhou Provinces, Southwest China. Ph.D. Thesis, China University of Geosciences, Beijing, China, 2013; pp. 1–167.
17. Cui, Z.; Liu, X.; Zhou, J. Fractal characteristics of faults and its geological significance in Sichuan-Yunnan-Guizhou Pb-Zn metallogenic province, China. *Glob. Geol.* **2021**, *40*, 75–92.
18. Han, R.; Liu, C.; Huang, Z.; Chen, J.; Ma, D.; Li, Y. Genesis modeling of Huize lead-zinc ore deposit in Yunnan. *Acta Mineral. Sin.* **2001**, *21*, 674–680.
19. Li, W.B.; Huang, Z.L.; Zhang, G. Sources of the ore metals of the Huize ore field in Yunnan province: Constraints from Pb, S, C, H, O and Sr isotope geochemistry. *Acta Petrol. Sin.* **2006**, *22*, 2567–2580.

20. Zhang, C.; Zhang, Z.L.; Huang, Z.L.; Yan, Z.F. Study on the sources of Pb and Zn in Huize lead-zinc ore deposits. *Gansu Geol.* **2008**, *17*, 26–31.
21. Han, R.; Chen, J.; Li, Y.; Ma, D.; Zhao, D.; Ma, G. Ore-controlling tectonics and prognosis of concealed ores in Huize Pb-Zn deposit, Yunnan. *Acta Mineral. Sin.* **2001**, *21*, 265–269.
22. Erik, F. *Carbonate Micro-Characteristics*; Geological Publishing House: Beijing, China, 2006.
23. Wang, C. Experimental Study on Mechanical Properties of Dolomite Limestone in Huize Lead-Zinc Mine. Master's Thesis, Kunming University of Science and Technology, Kunming, China, 2013.
24. Zhang, C.Q.; Mao, J.; Wu, S.P.; Li, H.M.; Liu, F.; Guo, B.J.; Gao, D.R. Distribution, characteristics and genesis of Mississippi valley-type lead-zinc deposits in Sichuan-Yunnan-Guizhou area. *Miner. Depos.* **2005**, *24*, 336–348.
25. Zhou, J.-X.; Xiang, Z.-Z.; Zhou, M.-F.; Feng, Y.-X.; Luo, K.; Huang, Z.-L.; Wu, T. The giant upper yangtze Pb–Zn province in SW China: Reviews, new advances and a new genetic model. *J. Asian Earth Sci.* **2018**, *154*, 280–315. [CrossRef]
26. Kong, Z.; Wu, Y.; Liang, T.; Zhang, F.; Meng, X.; Lu, L. Sources of ore-forming material for Pb-Zn deposits in the Sichuan-Yunnan-Guizhou triangle area: Multiple constraints from C-H-O-S-Pb-Sr isotopic compositions. *Geol. J.* **2018**, *53*, 159–177. [CrossRef]
27. Zhang, C.; Wu, Y.; Hou, L.; Mao, J. Geodynamic setting of mineralization of Mississippi Valley–type deposits in world–class Sichuan–Yunnan–Guizhou Zn–Pb triangle, Southwest China: Implications from age–dating studies in the past decade and the Sm–Nd age of Jinshachang deposit. *J. Asian Earth Sci.* **2015**, *103*, 103–114. [CrossRef]
28. Tu, G.Z. Two unique mineralization areas in southwest China. *Bull. Mineral. Petrol. Geochem.* **2002**, *21*, 1–2.
29. Han, R.; Hu, Y.; Wang, X.; Huang, Z.; Chen, J.; Wang, F.; Wu, P.; Li, B.; Wang, H.; Dong, L.; et al. Mineralization model of rich Ge-Ag-bearing Zn-Pb polymetallic deposit concentrated district in northeastern Yunnan, China. *Acta Geol. Sin.* **2012**, *86*, 280–294.
30. Zhou, J.X.; Huang, Z.L.; Lv, Z.C.; Zhu, X.K.; Gao, J.G.; Mirnejad, H. Geology, isotope geochemistry and ore genesis of the shanshulin carbonate-hosted Pb–Zn deposit, southwest China. *Ore Geol. Rev.* **2014**, *63*, 209–225. [CrossRef]
31. Li, H.; Zhang, C. The genetic relationship between the H_2S-bearing gas in Sichuan basin and lead-zinc-copper deposits around the basin. *Geol. Rev.* **2012**, *58*, 495–510.
32. Chen, J.; Han, R.S.; Gao, D.R.; Zhao, D.S. Geologicai characteristics of huize Pb-Zn deposit, yunnan and model of oreprospectibg method. *Earth Environ.* **2001**, 124–129.
33. Shi, X.W.; Jia, F.J.; Ke, L.Y.; Zou, C. The geochemical characteristics of the C-O isotope of the Huize mine area of Yunnan province, China. *Acta Mineral. Sin.* **2021**, *41*, 657–667.
34. Wang, Z.Q. Enrichment Regularity of Dispersed Elements in Huize Super-Large Pb-Zn Deposit. Master's Thesis, China University of Geosciences, Beijing, China, 2017; pp. 1–65.
35. Wardlaw, N.C.; Li, Y.; Forbes, D. Pore-throat size correlation from capillary pressure curves. *Transp. Porous Media* **1987**, *2*, 597–614. [CrossRef]
36. Wen, D.X.; Han, R.S.; Wu, P.; He, J.J. Altered dolomite features and petro-geochemical prospecting indicators in the Huize lead-zinc deposit. *Geol. China* **2014**, *41*, 235–245.
37. Manning, C.E.; Ingebritsen, S.E. Permeability of the continental crust: Implications of geothermal data and metamorphic systems. *Rev. Geophys.* **1999**, *37*, 127–150. [CrossRef]
38. McCreesh, C.A.; Eris, E.L.; Brumfield, D.S.; Ehrlich, R. *Relating Thin Sections to Permeability, Mercury Porosimetry, Formation Factor, and Tortousity*; American Association of Petroleum Geologists AAPG/Datapages: Tulsa, OK, USA, 1988.